

**Bismuth ferrite-based lead free ceramics and multilayers with high recoverable energy density**

WANG, Dawei, FAN, Zhongming, ZHOU, Di, KHESRO, Amir, MURAKAMI, Shunsuke, FETEIRA, Antonio <<http://orcid.org/0000-0001-8151-7009>>, ZHAO, Quanliang, TAN, Xiaoling and REANEY, Ian

Available from Sheffield Hallam University Research Archive (SHURA) at:

<http://shura.shu.ac.uk/18633/>

---

This document is the author deposited version. You are advised to consult the publisher's version if you wish to cite from it.

**Published version**

WANG, Dawei, FAN, Zhongming, ZHOU, Di, KHESRO, Amir, MURAKAMI, Shunsuke, FETEIRA, Antonio, ZHAO, Quanliang, TAN, Xiaoling and REANEY, Ian (2018). Bismuth ferrite-based lead free ceramics and multilayers with high recoverable energy density. *Journal of Materials Chemistry A*, 6 (9), 4133-4144.

---

**Copyright and re-use policy**

See <http://shura.shu.ac.uk/information.html>

**Bismuth ferrite-based lead free ceramics and multilayers  
with high recoverable energy density**

Journal:	<i>Journal of Materials Chemistry A</i>
Manuscript ID	TA-ART-11-2017-009857.R1
Article Type:	Paper
Date Submitted by the Author:	25-Jan-2018
Complete List of Authors:	Wang, Dawei; University of Sheffield, Department of Materials Science and Engineering Fan, Zhongming; Iowa State University Zhou, Di; University of Sheffield, Department of Materials Science and Engineering Khesro, Amir; University of Sheffield Murakami, Shunsuke ; University of Sheffield, Department of Materials Science and Engineering Feteira, Antonio ; Sheffield Hallam University, Zhao, Quanliang; North China University of Technology, Tan, Xiaoli; Iowa State University, Department of Material Science & Engineering Reaney, Ian; University of Sheffield, Engineering Materials



Journal Name

ARTICLE

## Bismuth ferrite-based lead free ceramics and multilayers with high recoverable energy density

Received 00th January 20xx,  
Accepted 00th January 20xx

DOI: 10.1039/x0xx00000x

www.rsc.org/

Dawei Wang,<sup>a\*</sup> Zhongming Fan,<sup>b</sup> Di Zhou,<sup>a,c</sup> Amir Khesro,<sup>a,d</sup> Shunsuke Murakami,<sup>a</sup> Antonio Feteira,<sup>e</sup> Quanliang Zhao,<sup>f</sup> Xiaoli Tan,<sup>b</sup> Ian M Reaney<sup>a\*</sup>

Lead-free ceramics with high recoverable energy density ( $W_{rec}$ ) and energy storage efficiency ( $\eta$ ) are attractive for advanced pulsed power capacitors to enable greater miniaturization and integration. In this work, dense bismuth ferrite (BF)-based, lead-free  $0.75(\text{Bi}_{1-x}\text{Nd}_x)\text{FeO}_3\text{-}0.25\text{BaTiO}_3$  (BNx-F-BT) ceramics and multilayers were fabricated. A transition from a mixed pseudocubic and  $R3c$  to a purely pseudocubic structure was observed as  $x$  increased with optimum properties obtained for mixed compositions. Highest energy densities,  $W \sim 4.1 \text{ J/cm}^3$  and  $W_{rec} \sim 1.82 \text{ J/cm}^3$  were achieved for BN15F-BT, due to the enhanced breakdown field strength (BDS  $\sim 180 \text{ kV/cm}$ ) and large maximum polarization ( $P_{max} \sim 40 \mu\text{C/cm}^2$ ). Multilayers of this composition possessed both high  $W_{rec}$  of  $6.74 \text{ J/cm}^3$  and  $\eta$  of 77% and were stable up to  $125 \text{ }^\circ\text{C}$ . Nd doped BF-based ceramics with enhanced BDS and large  $W_{rec}$  are therefore considered promising candidates for lead-free energy storage applications.

### Introduction

Materials with higher energy and power density are urgently needed to meet the growing power supply demand of portable electronics, power electronics, electrical vehicles and other energy storage devices.<sup>1-3</sup> Compared to other energy storage devices (such as fuel cells, batteries, and electrochemical capacitors), dielectric capacitors have received particular attention for advanced pulsed power because of their high power density and quick charge-discharge rate.<sup>4-7</sup> In general, three kinds of dielectric materials are used in capacitors: linear dielectrics; anti-ferroelectrics (AFE) and ferroelectrics (FE). For linear dielectrics energy density ( $W$ ) is defined as:

$$W = \frac{1}{2} DE = \frac{1}{2} \epsilon_r \epsilon_0 E^2, \quad (1)$$

where  $D$  is the electrical displacement,  $\epsilon_r$  is the dielectric constant,  $\epsilon_0$  is the vacuum permittivity and  $E$  is the applied-field. Both high  $\epsilon_r$  and  $E$  are required to achieve high  $W$  for

linear dielectrics. For AFE and FE,  $W$ , recoverable energy density ( $W_{rec}$ ) and energy storage efficiency ( $\eta$ ) are calculated by:

$$W = \int_0^{P_{max}} EdP, \quad (2)$$

$$W_{rec} = \int_{P_r}^{P_{max}} EdP, \quad (3)$$

$$\eta = W_{rec}/W \quad (4)$$

where  $P$ ,  $P_{max}$  and  $P_r$  is the polarization, maximum polarization and remnant polarization, respectively. To achieve high  $W_{rec}$  and  $\eta$ , large  $P_{max}$ , small  $P_r$  and high electric breakdown strength (BDS) are simultaneously required.

Currently, polymers and ceramics dominate the dielectric materials used in solid-state capacitors. However, polymer-based dielectrics with high  $W$  resulting from high BDS, are usually limited to  $<100^\circ\text{C}$ , due to their low melting temperatures.<sup>8,9</sup> Dielectric ceramics therefore, offer a viable option to develop high voltage-capable, high energy density, mechanically and thermally stable capacitors which operate at elevated temperatures. Lead-based dielectric ceramics have already proven to have potential in the application of energy-storage capacitors, with high  $W_{rec}$  ( $6.4 \text{ J/cm}^3$ ) reported in La-doped  $\text{Pb}(\text{Zr,Ti})\text{O}_3$ -based AFE ceramics fabricated by spark plasma sintering (SPS).<sup>10-15</sup> However, environmental issues, health concerns and regulations against hazardous substances in electric and electronic equipment have stimulated research in lead-free materials for energy-storage.<sup>16-18</sup>

Lead-free energy storage ceramics such as  $\text{BaTiO}_3$  (BT),  $(\text{Bi}_{0.5}\text{Na}_{0.5})\text{TiO}_3$  (BNT) and  $(\text{K}_{0.5}\text{Na}_{0.5})\text{NbO}_3$  (KNN)-based ceramics have been extensively investigated.<sup>19-31</sup> Initially, oxide additives such as  $\text{Al}_2\text{O}_3$ ,  $\text{SiO}_2$ ,  $\text{MgO}$  were reported to enhance the BDS and  $W_{rec}$  in BT-based ceramics<sup>20-22</sup> but more

<sup>a</sup> Department of Materials Science and Engineering, University of Sheffield, Sheffield S1 3JD, UK. \*E-mail: dawei.wang@sheffield.ac.uk, i.m.reaney@sheffield.ac.uk

<sup>b</sup> Department of Materials Science and Engineering, Iowa State University, Ames, Iowa, 50011 USA

<sup>c</sup> Electronic Materials Research Laboratory, Key Laboratory of the Ministry of Education & International Center for Dielectric Research, Xi'an Jiaotong University, Xi'an 710049, Shaanxi, China

<sup>d</sup> Department of Physics Abdul Wali Khan University, Garden Campus 23200, Mardan, Pakistan

<sup>e</sup> Christian Doppler Laboratory for Advanced Ferroic Oxides, Sheffield Hallam University, Sheffield S1 1WB, UK

<sup>f</sup> School of Mechanical and Materials Engineering, North China University of Technology, Beijing 100144, China

† Electronic Supplementary Information (ESI) available: [details of any supplementary information available should be included here]. See DOI: 10.1039/x0xx00000x

recently BT-Bi(M<sub>2/3</sub>Nb<sub>1/3</sub>)O<sub>3</sub> and BT-Bi(M<sub>1/2</sub>Ti<sub>1/2</sub>)O<sub>3</sub> (M = Mg and Zn) ceramics were studied, in which  $W_{rec}$  was reported up to 1~2 J/cm<sup>3</sup>.<sup>23-27</sup> In addition, Bi<sub>0.5</sub>Na<sub>0.5</sub>TiO<sub>3</sub>-BaTiO<sub>3</sub>-KNbO<sub>3</sub> (BNT-BT-KN) and Bi<sub>0.5</sub>Na<sub>0.5</sub>TiO<sub>3</sub>-BaTiO<sub>3</sub>-NaTaO<sub>3</sub> (BNT-BT-NT) ceramics were also reported to achieve high  $W_{rec}$  of 1.72 and 1.2 J/cm<sup>3</sup>, respectively.<sup>28,29</sup> Recently, Du et al. obtained very high BDS (300~400kV/cm) in KNN-based ceramics by controlling grain growth; hence  $W_{rec}$  was enhanced to ~ 4 J/cm<sup>3</sup>.<sup>30,31</sup> BiFeO<sub>3</sub>-BaTiO<sub>3</sub> (BF-BT) has been shown to have high Curie temperature ( $T_c$ ) and a large polarization at its structural phase boundary ( $P_{max} > 40 \mu\text{C}/\text{cm}^2$ ).<sup>32-35</sup> However, due to its high dielectric loss and  $P_r$ , the energy storage properties of BF-BT have rarely been studied. Recently, Wang and Zheng et al. introduced Nb, Ba(Mg<sub>1/3</sub>Nb<sub>2/3</sub>)O<sub>3</sub> and La(Mg<sub>1/2</sub>Ti<sub>1/2</sub>)O<sub>3</sub> into BF-BT and reported  $W_{rec}$  of 0.71, 1.56 and 1.66 J/cm<sup>3</sup>, respectively, suggesting that BF-BT solid solutions are promising candidates for energy storage materials and devices.<sup>36-38</sup> More recently, Xu et al. theoretically predicted that Nd-doped BF based ceramics could potentially allow high energy densities (100-150 J/cm<sup>3</sup>) and efficiencies (80-88%).<sup>39</sup> However, to our knowledge, there is no reported experimental work on the effect of Nd doping on the energy storage properties of BF-based systems. The composition dependence of structural, dielectric, ferroelectric, high-field strain and energy storage of Nd doped BF-BT ceramics and multilayers are therefore investigated. Multilayers fabricated with Pt internal electrodes yielded  $W_{rec}$  of 6.74 J/cm<sup>3</sup> and  $\eta$  of 77%, with the variation of  $W_{rec}$  ~ 15% from room temperature (RT) to 125 °C.

## Experimental

BF-BT ceramics with compositions of 0.75(Bi<sub>1-x</sub>Nd<sub>x</sub>)FeO<sub>3</sub> - 0.25BaTiO<sub>3</sub> + 0.1wt% MnO<sub>2</sub> (x = 0, 2.5%, 5%, 7.5%, 10%, 15%, 20%, 30% and 40%, abbreviated as BF-BT, BN2.5F-BT, BN5F-BT, BN7.5F-BT, BN10F-BT, BN15F-BT, BN20F-BT, BN30F-BT and BN40F-BT, respectively) were prepared using a conventional solid state reaction route. Multilayers were tapecast with details of ceramic and multilayer fabrication reported elsewhere.<sup>32,40</sup> Densities of sintered samples were measured using the Archimedes method. The structure and phase assemblage of the sintered samples were studied using a Bruker D2 Phaser X-ray powder diffraction (XRD). FEI Inspect F scanning electron microscope (SEM) and Tecnai G2-F20 transmission electron microscopy (TEM) were employed to reveal the grain and domain structure, respectively. For TEM, sintered pellets of BF-BT, BN5F-BT and BN10F-BT were mechanically ground and polished to 120  $\mu\text{m}$ . Disks of 3 mm in diameter were ultrasonically cut and the center portion was thinned to 10  $\mu\text{m}$  by mechanical dimpling. Disks were annealed at 550 °C, 400 °C and 300 °C for 0.5 hour to remove residual stresses followed by Ar-ion milling to the point of electron transparency. For electrical tests, sintered samples were electroded using fired-on silver paste, followed by poling in silicone oil at 100~120 °C with an applied electric field of ~ 60 kV/cm. The piezoelectric coefficient ( $d_{33}$ ) was measured using a Piezotest PM300  $d_{33}$  meter. Polarization hysteresis,

leakage current density and strain-electric field behaviour were determined using an aixACCT TF 2000E ferroelectric tester at a frequency of 1 Hz from RT to 150 °C. The displacement data was synchronously captured by a laser interferometer. The temperature dependence of dielectric properties from RT to 600 °C was carried out using an Agilent 4184A multi-frequency precision LCR meter. The discharge properties were measured using a specially designed, high-speed capacitor discharge circuit similar to that reported in the literature.<sup>19</sup> The discharge current waveforms were obtained by an Tektronix DPO 4104 oscilloscope connected with a Pearson 6585 coil. The discharge energy was measured using a load resistor (RL) in series with the ceramic samples.

## Results and discussion

The RT XRD patterns of BN<sub>x</sub>F-BT in the  $2\theta$  range of 20°~70° are shown in Fig. 1. All peaks were attributed to either a single or mixed perovskite phases. Diffraction peaks shifted to a higher diffraction angle with increasing Nd concentration, consistent with the smaller relative ionic radius of Nd<sup>3+</sup> with respect to Bi<sup>3+</sup> in the matrix.<sup>41,42</sup> Splitting of (021)/(110) diffraction peak at  $\sim 2\theta = 32^\circ$  is commonly used to determine the likely symmetry of compositions. From the expanded XRD patterns, the coexistence of two perovskite phases in the BF-BT, BN2.5F-BT and BN5F-BT is apparent at RT, as indicated by broad multiple peaks.<sup>32,34</sup> With increase in Nd concentration, a single pseudocubic (PC) phase gradually dominates.<sup>32-34</sup>

To further confirm structural evolution, Rietveld refinement of all studied compositions was performed using the GSAS+EXPGUI package,<sup>43,44</sup> in which a two-phase refinement ( $R3c + Pm\bar{3}m$ ) was used. Good agreement between the observed and calculated patterns was obtained for all the compositions as shown in Table I and Fig. 2, in which the refinements of BF-BT and BN10F-BT were selected for comparison (Fig. 2a,b). As Nd concentration increased, the fraction of  $R3c$  phase in BNF-BT decreased from 65.2% for BF-BT to 27.9% for BN5F-BT and to 0 for higher Nd concentration (Table I), indicating the coexistence of  $R$  and  $PC$  phases with  $x \leq 5\%$  and a single  $PC$  phase with  $x > 5\%$ . The unit cell volume of both  $R$  and  $PC$  phases decreased with increasing Nd concentration (Fig. 2c), consistent with a shift of XRD diffraction peaks to increasing  $2q$  (Fig. 1). There is an abrupt change in the lattice parameters of  $R3c$  phase for BN5F-BT (Fig. 2d). Whilst this does not indicate classic morphotropic phase boundary behaviour which is between two polar phases of different symmetry,<sup>45</sup> it implies a sharp rather than gradual loss of long range polar order as Nd concentration increases.

TEM images and selected area electron diffraction patterns (SADP) of BF-BT, BN5F-BT and BN10F-BT obtained with the electron parallel with a  $\langle 110 \rangle$  axis are shown in Fig. 3 and Fig. 4. In BF-BT, the domain structure is complex with coarse herringbone-type domains separated by 71° domain walls on  $\{110\}$  planes, fine herringbone-type domains separated by 109° domain walls on  $\{001\}$  planes and complex submicron-sized domains.<sup>46</sup> An example of the fine herringbone macrodomain structure is given in Fig 3. In BN5F-BT, 80% of

grains contain only nano-sized domains with the rest consisting of nano-sized and complex microdomains (Fig. 3), confirming its dominant pseudocubic nature. In contrast, all grains observed in BN10F-BT appeared domain-free (Fig. 3). In BF-BT,  $\frac{1}{2}\{000\}$  superlattice diffraction spots (Fig. 4) are observed which arise from rotations of the oxygen octahedra in antiphase, consistent with  $R3c$  symmetry with an  $a^-a^-a^-$  tilt system<sup>47</sup> and with Rietveld refinements (Fig. 1 and 2 and Table I). Although the  $\frac{1}{2}\{000\}$  superlattice reflections in BN5F-BT are weaker than those in BF-BT (Fig. 4), they are still discrete (Fig. 4), which indicates shorter correlation length and/or lesser magnitude of oxygen octahedral rotation in nano-sized regions in BN5F-BT with respect to the micron/submicron-sized domains in BF-BT. Despite the absence of an apparent domain structure,  $\frac{1}{2}\{000\}$  type superlattice reflections are still observed in SADPs (Fig. 4), albeit weak and diffuse, typical of short range order octahedral rotations. The ionic radius of Nd (1.27 Å) is smaller than that of Bi (1.35 Å)<sup>48</sup> and consequently the driving force for octahedral tilting (magnitude of octahedral rotation) according to tolerance factor arguments should increase and not decrease.<sup>49</sup> The decrease in intensity of the  $\frac{1}{2}\{000\}$  superstructure reflection may therefore only be explained by frustration between the competing local structures. In BiFeO<sub>3</sub>, the polar distortion is strongly coupled to the commensurate rotation of the octahedral cage around the [111] axis.<sup>50,51</sup> As the scale length of polar coupling decreases (as Nd concentration increases), so does the scale length of the octahedral rotations. Presumably, if the Nd concentration increases significantly further, long range octahedral tilting will re-emerge but most likely with a different tilt configuration, similar or related to that of the orthoferrites ( $a^-a^-c^+$ ).<sup>52</sup>

The SEM images of BNx<sub>F</sub>-BT are shown in Fig. 5. All ceramics appear dense and pore-free, presenting a grain size distribution, in which small grains are interspaced with large grains. Based on the SEM images, the grain size distributions of BNx<sub>F</sub>-BT are given in the insets of Fig. 5, and the average grain size and relative density ( $\rho_r$ ) of BNx<sub>F</sub>-BT as a function of Nd concentration is shown in Fig. 6. As Nd concentration increases, the grain size of BNx<sub>F</sub>-BT increases from 6.3 μm for BF-BT to 7.4 μm for BN2.5F-BT and then decreases to 1.9 μm for BN40F-BT, suggesting that high concentrations of Nd inhibit grain growth, possibly due to the more refractory nature of Nd<sub>2</sub>O<sub>3</sub>.<sup>34</sup> At the same time,  $\rho_r$  improves from 95% for BF-BT to 97.6% for BN20F-BT but then remains constant with increasing Nd concentration. Small grain size and high density in bulk ceramics are believed to lead to high BDS which in turn enhances energy density.

The temperature dependence of dielectric permittivity ( $\epsilon_r$ ) and loss ( $\tan\delta$ ) for BNx<sub>F</sub>-BT at 100 kHz is given in Fig. 7, with the corresponding  $T_c$ / maximum transition temperature ( $T_m$ ) as a function of Nd concentration given in the inset of Fig. 7(b). With increasing Nd concentration,  $T_c/T_m$  decreases presumably due to the disruption of polar coupling by the substitution of the less polarisable Nd for Bi.<sup>32,33</sup> The decrease in polar coupling is also manifested in the appearance of broad frequency-dependent dielectric peaks, in agreement with the nano-sized domains in TEM images (Fig. 3). Despite these

changes, the values of  $\tan\delta$  remain  $< 0.15$  at  $< 300$  °C, but then increase sharply (Fig. 7b), indicating an increase in dc conductivity at high temperature.

The high electric field bipolar polarization hysteresis (P-E) and unipolar strain (S-E) loops of BNx<sub>F</sub>-BT samples are shown in Fig. 8(a,b) (the strain of BNx<sub>F</sub>-BT with  $x > 15\%$  was too low to be detected), from which  $P_r$ , coercive field ( $E_c$ ) and average electric field induced maximum strain ( $S_{max}$ ) as a function of Nd concentration are obtained. The effective high field piezoelectric strain coefficient ( $d_{33}^*$ ) and hysteresis ( $SH$ ) are calculated by

$$d_{33}^* = S_{max}/E_{max}, \quad (5)$$

$$SH = H_{E_{max}/2}/S_{max}, \quad (6)$$

respectively, where  $E_{max}$  is the maximum electric field value,  $H_{E_{max}/2}$  is the width of the loop at half applied field.<sup>53</sup> Samples of BF-BT and BN2.5F-BT give saturated hysteresis loops (Fig. 8a) at 70 kV/cm, indicating high resistivity. As Nd concentration increased, the P-E loops became slimmer and unsaturated (Fig. 8a), with  $P_r$ ,  $E_c$  and  $d_{33}$  continuously decreasing (Fig. 8c), indicative of relaxor-like behaviour, consistent with the broad permittivity maximum (Fig. 7a) and domain evolution (Fig. 3). The highest value of  $P_r \sim 35$  μC/cm<sup>2</sup>,  $E_c \sim 53.9$  kV/cm,  $d_{33} \sim 140$  pC/N and lowest value of  $HS \sim 18.4\%$  is achieved for the 2.5%Nd doped BF-BT (Fig. 8c,d), due to the presence of mixed  $R3c$  and  $PC$  phases (Fig. 1 and 2).<sup>32-34</sup> At the same time, the highest value of  $S_{max} \sim 0.14\%$ ,  $d_{33}^* \sim 200$  pm/V and  $HS \sim 50\%$  was obtained for BN5F-BT, Fig. 8(c, d), mainly attributed to the crossover from normal to relaxor ferroelectric behaviour (Fig. 3 and 7).<sup>32</sup>

Due to their slim P-E loops with low hysteresis loss (Fig. 7a), BNx<sub>F</sub>-BT with  $x > 10\%$  were selected and polished to  $\sim 0.3$  mm for further studies on their potential for energy storage. Unipolar P-E loops under different electric fields for BNx<sub>F</sub>-BT ( $x > 10\%$ ) are shown in Fig. 9 with the corresponding values of  $P_{max}$ ,  $P_r$  and  $\Delta P$  ( $P_{max} - P_r$ ) as a function of electric field given in Fig. 10. As electric field increases,  $P_{max}$  and  $\Delta P$  increase linearly with a slight increase of  $P_r$  for all studied compositions (Fig. 10). However,  $P_{max}$ ,  $P_r$  and  $\Delta P$  decrease at 170 kV/cm with increasing Nd concentration (in the inset of Fig. 10d), further confirming that Nd doping reduces polarization in BF-BT ceramics (Fig. 8a). The highest values of  $P_{max}$  and  $\Delta P$  are 39.8, 23.5, 11.6, 7.8 μC/cm<sup>2</sup> and 30.7, 20.4, 10.7, 7.6 μC/cm<sup>2</sup> for BN15F-BT, BN20F-BT, BN30F-BT and BN40F-BT, respectively.

The energy storage properties  $W$ ,  $W_{rec}$  and  $\eta$  are calculated from equations 2-4, given in Fig. 11. With increasing electric field, the values of  $W$  and  $W_{rec}$  increase for all studied compositions (Fig. 11a,b), the highest values of which are 4.1, 2.43, 1.16, 0.75 J/cm<sup>3</sup> and 1.82, 1.53, 0.87, 0.66 J/cm<sup>3</sup>, respectively. At the same time, the values of  $\eta$  slightly decrease for BN15F-BT, BN30F-BT and BN40F-BT but increase for BN20F-BT (Fig. 11c). As Nd concentration increases,  $W$  and  $W_{rec}$  decrease significantly at an electric field of 170 kV/cm, with the values of  $\eta$  reaching a maximum of 87.8% for BN40F-BT (Fig. 11d).

A comparison of energy-storage properties among several lead-free FE and multiferroic ceramics is given in Table II. BN15F-BT has the highest values of  $P_{max} \sim 39.8 \mu\text{C}/\text{cm}^2$ ,  $W \sim 4.1 \text{ J}/\text{cm}^3$  and  $W_{rec} \sim 1.82 \text{ J}/\text{cm}^3$  among all displayed lead-free ferroelectric ceramics with an electric field  $< 250 \text{ kV}/\text{cm}$ . BN20F-BT has high values of  $W \sim 2.43 \text{ J}/\text{cm}^3$  and  $W_{rec} \sim 1.53 \text{ J}/\text{cm}^3$  with a medium value of  $\eta \sim 63\%$ , whilst the values of  $W$  and  $W_{rec}$  for BN30F-BT and BN40F-BT are low but with much higher values of  $\eta (> 75\%)$ . According to equations 2 and 3, the large values of  $W \sim 4.1 \text{ J}/\text{cm}^3$  and  $W_{rec} \sim 1.82 \text{ J}/\text{cm}^3$  for BN15F-BT may be attributed to the higher BDS ( $180 \text{ kV}/\text{cm}$ ),  $P_{max}$  ( $39.8 \mu\text{C}/\text{cm}^2$ ) and  $\Delta P$  ( $30.7 \mu\text{C}/\text{cm}^2$ ), as discussed in Fig. 10. The BDS of bulk ceramics is related to microstructural features, such as grain size, density (porosity), grain boundary and secondary phase. Tunkasiri et al. confirmed the relationship between BDS and grain size ( $G$ ) of ceramics (equ. 7).<sup>54</sup>

$$\text{BDS} \propto \frac{1}{\sqrt{G}} \quad (7)$$

Gerson et al. and Wu et al. reported that the BDS of dielectric ceramics would reduce greatly with an increase in porosity and defects.<sup>55,56</sup> In this work, significant reduction of grain size and porosity is achieved by doping with Nd (Figs. 5 and 6), leading to a large BDS of  $\sim 180 \text{ kV}/\text{cm}$  for BN15F-BT and  $\sim 190 \text{ kV}/\text{cm}$  for BN20F-BT, BN30F-BT and BN40F-BT, respectively; the highest values of BDS in all reported BF-based bulk ceramics to our knowledge.<sup>36-38</sup> Furthermore, BF-based solid solutions possess intrinsically large  $P_{max}$  which increases for relaxor ferroelectrics with increase in electric field.<sup>30,32-35</sup> Consequently, the improvement in  $W$  and  $W_{rec}$  for BNx-F-BT is attributed to both the large BDS and high  $P_{max}$  induced by Nd doping.

Owing to its promising energy storage properties in bulk samples, BN15F-BT was co-fired with Pt internal electrodes at  $1010\text{-}1040^\circ\text{C}$  for 2hrs to form multilayers consisting of 9 active layers, as shown in the inset of Fig. 12(a). The total thickness of multilayers is  $\sim 0.78 \text{ mm}$ , the thickness of each sintered layer is  $\sim 32 \mu\text{m}$  and the active area of each electrode is  $\sim 33 \text{ mm}^2$ . The unipolar P-E loops under different electric fields at RT and the *in-situ* temperature dependence of unipolar P-E loops at an electric field of  $300 \text{ kV}/\text{cm}$  per layer are shown in Fig. 12(a, b), respectively. The corresponding values of  $P_{max}$ ,  $P_r$  and  $\Delta P$  as a function of electrical field and temperature are given in Fig. 13. The energy storage properties  $W$ ,  $W_{rec}$  and  $\eta$  are also calculated and plotted in Fig. 12(c,d). With increase in electric field, the shape of P-E loops becomes slimmer, and the values of  $P_{max}$  and  $\Delta P$  increase significantly with a slight increase in  $P_r$  (Fig. 13a), resulting in enhanced values of  $W$ ,  $W_{rec}$  and  $\eta$  (Fig. 12c). The highest values of  $W \sim 8.75 \text{ J}/\text{cm}^3$ ,  $W_{rec} \sim 6.74 \text{ J}/\text{cm}^3$  and  $\eta \sim 77\%$  for multilayers are obtained with an electric field of  $540 \text{ kV}/\text{cm}$ , which is one of the highest reported energy densities for ceramic capacitors.<sup>57-60</sup> As temperature increased, P-E loops become saturated at  $\sim 150^\circ\text{C}$ , leading to an increase of  $P_{max}$  and  $P_r$  (Fig. 13b), which is attributed to an easier field induced transition from a relaxor to a ferroelectric state.<sup>32</sup> The value of  $W$  consistently increases with temperature, while  $W_{rec}$  and  $\eta$  increases initially before decreasing after reaching maxima of  $3.84 \text{ J}/\text{cm}^3$  and  $76\%$  at  $100^\circ\text{C}$ , Fig. 12(d). The

variation in  $W_{rec}$  is  $\sim 15\%$  in a temperature range between RT and  $125^\circ\text{C}$ , which is attractive for commercial applications.

The *in-situ* temperature dependence of leakage current density ( $J$ ) of multilayers as a function of applied field is shown in Fig. 14. The value of  $J$  at RT is found to be on the order of  $10^{-7} \text{ A}/\text{cm}^2$  in the high field region, which is at least one order smaller than that reported BF-based ceramics.<sup>61,62</sup> With the increase of temperature from RT to  $150^\circ\text{C}$ , the value of  $J$  consistently increases, indicating increased conductivity at high temperatures.

The discharge behaviour of multilayers under different electric voltages is given in Fig. 15. The value of current is found to increase with the increase of voltage from  $300 \text{ V}$  to  $900 \text{ V}$  and all the discharge processes last about  $10 \mu\text{s}$ , as shown in Fig. 15(a). The discharge time  $\tau_{0.9}$  is defined as the time for the discharge energy in the load to achieve 90% of the final value from the discharge profiles, which could be obtained from the curves of discharge energy density as a function of discharge time (Fig. 15b). The  $\tau_{0.9}$  of multilayers under different voltages is less than  $4 \mu\text{s}$ , indicating that 90% of the discharge energy density is released with this time period.

A comparison of  $W_{rec}$  and  $\eta$  among lead-based and lead-free ceramics/capacitors is summarized and plotted in Fig. 16.  $W_{rec}$  generally increases with electric field (Fig. 16a), while  $\eta$  decreases with larger values of  $W_{rec}$  (Fig. 16b). Lead-based ceramics still have higher values of  $W_{rec}$  compared to the lead-free ceramics (Fig. 16a) but the multilayers fabricated in this contribution possess the largest value of  $W_{rec} \sim 6.74 \text{ J}/\text{cm}^3$  with high  $\eta \sim 77\%$  amongst lead-based and lead-free compositions at  $< 600 \text{ kV}/\text{cm}$  (Fig. 16).

## Conclusions

In this work, dense Nd doped BF-BT lead-free ceramics with  $\rho_r \geq 95\%$  were prepared using a conventional solid state route. As Nd concentration increased, the BF-BT gradually transformed from a two phase mix of  $R3c$  and  $PC$  phases to a single  $PC$  phase, accompanied by a decrease of  $T_C/T_m$  and ferroelectric/piezoelectric/strain properties. The domain structure gradually altered in a manner consistent with the change in structure and phase assemblage from coarse herringbones-type domains, fine herringbones-type domains and complex domains to nano-sized domains and finally to a nominally domain free state. This was accompanied by a reduction in the intensity of  $\frac{1}{2}\{000\}$  superstructure reflections associated with octahedral tilting, despite a decrease in the average tolerance factor as Nd concentration increased. This unusual effect is attributed to frustration of long range tilting due to competing local distortions (phases) within the solid solution. The highest values of  $d_{33} \sim 140 \text{ pC}/\text{N}$ ,  $P_r \sim 35 \mu\text{C}/\text{cm}^2$ ,  $E_C \sim 53.9 \text{ kV}/\text{cm}$ ,  $S_{max} \sim 0.14\%$  and  $d_{33}^* = 200 \text{ pm}/\text{V}$  were obtained for the compositions with Nd concentration  $< 7.5\%$ . Furthermore, the average grain size of BNF-BT was reduced from  $6.3 \mu\text{m}$  for BF-BT to  $1.9 \mu\text{m}$  for BN40F-BT, with an increase of  $\rho_r$  from  $95\%$  for BF-BT to  $97.6\%$  for BN40F-BT, leading to high BDS ( $180 \text{ kV}/\text{cm}$  for BN15F-BT and  $190 \text{ kV}/\text{cm}$  for

for BN20F-BT, BN30F-BT, BN40F-BT) and large  $P_{max}/\Delta P$  (39.8, 23.5, 11.6, 7.8  $\mu\text{C}/\text{cm}^2$  and 30.7, 20.4, 10.7, 7.6  $\mu\text{C}/\text{cm}^2$  for BN15F-BT, BN20F-BT, BN30F-BT and BN40F-BT, respectively). As electric field increased,  $W$  and  $W_{rec}$  increased for all studied compositions, with  $\eta$  changing only slightly. As Nd concentration increased,  $W$  and  $W_{rec}$  decreased significantly, with  $\eta$  increasing greatly. The largest values of  $W \sim 4.1 \text{ J}/\text{cm}^3$  and  $W_{rec} \sim 1.82 \text{ J}/\text{cm}^3$  were achieved for BN15F-BT, while the maximum  $\eta$  of 87.8% was obtained for BN40F-BT. BN15F-BT multilayers consisting of 9 active layers were fabricated. The highest values of  $W \sim 8.75 \text{ J}/\text{cm}^3$ ,  $W_{rec} \sim 6.74 \text{ J}/\text{cm}^3$  and  $\eta \sim 77\%$  were obtained at an electric field of 540 kV/cm, with a variation of  $\sim 15\%$  for the value of  $W_{rec}$  from RT to 125 °C, values attractive for commercial applications.

### Conflicts of interest

There are no conflicts to declare.

### Acknowledgements

We acknowledge the Engineering and Physical Sciences Research Council (EP/N010493/1 and EP/L017563/1) and National Natural Science Foundation of China (51402005) for funding and supporting this work.

### References

- C. Liu, F. Li, L. P. Ma and H. M. Cheng, *Adv. Mater.*, 2010, **22**, E28.
- I. Hadjipaschalis, A. Poullikkas and V. Efthimiou, *Renew. Sust. Energy Rev.*, 2009, **13**, 1513.
- H. Chen, T. N. Cong, W. Yang, C. Tan, Y. Li and Y. Ding, *Prog. Nat. Sci.*, 2009, **19**, 291.
- G. R. Love, *J. Am. Ceram. Soc.*, 1990, **73**, 323.
- S. Kwon, W. Hackenberger, E. Alberta, E. Furman and M. Lanagan, *IEEE Electr. Insul. Mag.*, 2011, **27**, 43.
- W. B. Hu, Y. Liu, R. L. Withers, T. J. Frankcombe, L. Noren, A. Snashall, M. Kitchin, P. Smith, B. Gong, H. Chen, J. Schiemer, F. Brink and J. W. Leung, *Nat. Mater.*, 2013, **12**, 821.
- Q. Li, G. Zhang, F. Liu, K. Han, M. R. Gadinski, C. Xiong and Q. Wang, *Energy Environ. Sci.*, 2015, **8**, 922.
- B. Chu, X. Zhou, K. Ren, B. Neese, M. Lin, Q. Wang, F. Bauer and Q. M. Zhang, *Science*, 2006, **313**, 334.
- Q. Li, L. Chen, M. R. Gadinski, S. Zhang, G. Zhang, H. Li, A. Haque, L. Chen, T. Jackson and Q. Wang, *Nature*, 2015, **523**, 567.
- L. Zhang, S. Jiang, B. Fan and G. Zhang, *J. Alloys Compd.*, 2015, **622**, 162.
- Z. Liu, X. Chen, W. Peng, C. Xu, X. Dong, F. Cao, and G. Wang, *Appl. Phys. Lett.*, 2015, **106**, 262901.
- Q. Zhang, H. Tong, J. Chen, Y. Lu, T. Yang, X. Yao, and Y. He, *Appl. Phys. Lett.*, 2016, **109**, 262901.
- R. Xu, B. Li, J. Tian, Z. Xu, Y. Feng, X. Wei, D. Huang, and L. Yang, *Appl. Phys. Lett.*, 2017, **110**, 142904.
- Q. Zhang, J. Chen, Y. Lu, T. Yang, X. Yao, and Y. He, *J. Am. Ceram. Soc.*, 2016, **99**, 3853.
- Q. L. Zhao, H. Lei, G. P. He, J. J. Di, D. W. Wang, P. P. Tan, H. B. Jin and M. S. Cao, *Ceram. Int.*, 2016, **42**, 1314.
- J. Rodel, K. G. Webber, R. Dittmer, W. Jo, M. Kimura and D. Damjanovic, *J. Eur. Ceram. Soc.*, 2015, **35**, 1659.
- J. G. Wu, D. Q. Xiao and J. G. Zhu, *Chem. Rev.*, 2015, **115**, 2559.
- D. W. Wang, F. Hussain, A. Khesro, A. Feteira, Y. Tian, Q. L. Zhao and I. M. Reaney, *J. Am. Ceram. Soc.*, 2017, **100**, 627.
- W. B. Li, D. Zhou, L. X. Pang, R. Xu and H. H. Guo, *J. Mater. Chem. A*, 2017, **5**, 19607.
- B. B. Liu, X. H. Wang, Q. C. Zhao and L. T. Li, *J. Am. Ceram. Soc.*, 2015, **98**, 2641.
- Q. M. Zhang, L. Wang, J. Luo, Q. Tang, and J. Du, *Int. J. Appl. Ceram. Technol.*, 2010, **7**, E124.
- Y. H. Huang, Y. J. Wu, W. J. Qiu, J. Li and X. M. Chen, *J. Eur. Ceram. Soc.*, 2015, **35**, 1469.
- W. B. Li, D. Zhou and L. X. Pang, *Appl. Phys. Lett.*, 2017, **110**, 132902.
- T. Wang, L. Jin, C. C. Li, Q. Y. Hu and X. Y. Wei, *J. Am. Ceram. Soc.*, 2015, **98**, 559.
- Q. Y. Hu, L. Jin, T. Wang, C. C. Li, Z. Xing and X. Y. Wei, *J. Alloys Compd.*, 2015, **640**, 416.
- Z. B. Shen, X. H. Wang, B. C. Luo and L. T. Li, *J. Mater. Chem. A*, 2015, **3**, 18146.
- L. W. Wu, X. H. Wang and L. T. Li, *RSC Adv.*, 2016, **6**, 14273.
- Q. Xu, J. Xie, Z. C. He, L. Zhang, M. H. Cao, X. D. Huang, M. T. Lanagan, H. Hao, Z. H. Yao, H. X. Liu, *J. Eur. Ceram. Soc.*, 2017, **37**, 99.
- Q. Xu, H. X. Liu, L. Zhang, J. Xie, H. Hao, M. H. Cao, Z. H. Yao and M. T. Lanagan, *RSC Adv.*, 2016, **6**, 59280.
- Z. T. Yang, H. L. Du, S. B. Qu, Y. D. Hou, H. Ma, J. F. Wang, J. Wang, X. Y. Wei and Z. Xu, *J. Mater. Chem. A*, 2016, **4**, 13778.
- T. Q. Shao, H. L. Du, H. Ma, S. B. Qu, J. Wang, J. F. Wang, X. Y. Wei and Z. Xu, *J. Mater. Chem. A*, 2017, **5**, 554.
- D. W. Wang, A. Khesro, S. Murakami, A. Feteira, Q. L. Zhao and I. M. Reaney, *J. Eur. Ceram. Soc.*, 2017, **37**, 1857.
- Q. J. Zheng, L. L. Luo, K. H. Lam, N. Jiang, Y. Q. Guo and D. M. Lin, *J. Appl. Phys.*, 2014, **116**, 184101.
- M. H. Lee, D. J. Kim, J. S. Park, S. W. Kim, T. K. Song, M. H. Kim, W. J. Kim, D. Do and I. K. Jeong, *Adv. Mater.*, 2015, **27**, 6976.
- H. B. Yang, C. R. Zhou, X. Y. Liu, Q. Zhou, G. H. Chen, W. Z. Li and H. Wang, *J. Eur. Ceram. Soc.*, 2013, **33**, 1177.
- T. Wang, L. Jin, Y. Tian, L. L. Shu, Q. Y. Hu and X. Y. Wei, *Mater. Lett.*, 2014, **137**, 79.
- D. G. Zheng, R. Z. Zuo, D. S. Zhang and Y. Li, *J. Am. Ceram. Soc.*, 2015, **98**, 2692.
- D. G. Zheng and R. Z. Zuo, *J. Eur. Ceram. Soc.*, 2017, **37**, 413.
- B. Xu, J. Iniguez and L. Bellaiche, *Nat. Commun.*, 2017, **8**, 15682.
- A. Khesro, D. W. Wang, F. Hussain, D. C. Sinclair, A. Feteira, and I. M. Reaney, *Appl. Phys. Lett.*, 2016, **109**, 142907.
- D. W. Wang, M. L. Wang, F. B. Liu, Y. Cui, Q. L. Zhao, H. Sun, H. B. Jin and M. S. Cao, *Ceram. Int.*, 2015, **41**, 8768.
- Y. Li, W. Q. Cao, J. Yuan, D. W. Wang and M. S. Cao, *J. Mater. Chem. C*, 2015, **3**, 9276.
- C. Larson and R. B. Von Dreele, Los Alamos: Los Alamos National Laboratory Report LAUR; 2004.
- H. Toby, *J. Appl. Cryst.*, 2001, **34**, 210.
- B. Jaffe, W. R. Cook, and H. Jaffe, Piezoelectric Ceramics. Academic, London-New York, 1971.
- C. W. Huang, L. Chen, J. Wang, Q. He, S. Y. Yang, Y. H. Chu, R. Ramesh, *Phys. Rev. B*, 2009, **80**, 140101.
- D. I. Woodward, I. M. Reaney, *Acta Cryst.*, 2005, **61**, 387-399.
- R. D. Shannon, *Acta Cryst.*, 1976, **A32**, 751.
- S. Karimi, I. M. Reaney, I. Levin, I. Sterianou, *Appl. Phys. Lett.*, 2009, **94**, 112903.
- D. C. Arnold, K. S. Knight, F. D. Morrison, P. Lightfoot, *Phys. Rev. Lett.*, 2009, **102**, 027602.
- P. M. Woodward, *Acta Cryst.*, 1997, **853**: 44.
- S. Karimi, I. M. Reaney, Y. Han, J. Pokorny, I. Sterianou, *J. Mater. Sci.*, 2009, **19**, 5102.

## ARTICLE

Journal Name

- 53 D. W. Wang, M. S. Cao and S. J. Zhang, *J. Am. Ceram. Soc.*, 2012, **95**, 3220.
- 54 T. Tunkasiri and G. Rujijanagul, *J. Mater. Sci. Lett.*, 1996, **15**, 1767.
- 55 R. Gerson and T.C. Marshall, *J. Appl. Phys.*, 1959, **30**, 1650.
- 56 Y. J. Wu, Y. H. Huang, N. Wang, J. Li, M. S. Fu and X. M. Chen, *J. Eur. Ceram. Soc.*, 2017, **7**, 2099.
- 57 H. Ogihara, C. A. Randall and S. Trolrier-McKinstry, *J. Am. Ceram. Soc.*, 2009, **92**, 1719.
- 58 Y. Gao, H. X. Liu, Z. H. Yao, H. Hao, Z. Y. Yu and M. H. Cao, *Ceram. Inter.*, 2017, **43**, 8418.
- 59 D. P. Shay, N. J. Podraza, N. J. Donnelly and C. A. Randall, *J. Am. Ceram. Soc.*, 2012, **95**, 1348.
- 60 H. Lee, J. R. Kim, M. J. Lanagan, S. Trolrier-McKinstry and C. A. Randall, *J. Am. Ceram. Soc.*, 2013, **96**, 1209.
- 61 Y. Guo, P. Xiao, R. Wen, Y. Wan, Q. Zheng, D. Shi, K. H. Lam, b M. Liu and D. Lin, *J. Mater. Chem. C*, 2015, **3**, 5811.
- 62 N. Liu, R. Liang, Z. Liu, Z. Zhou, C. Xu, G. Wang, X. Dong, *Appl. Phys. Lett.*, 2017, **110**, 112902.
- 63 H. Tao, W. Wu and J. G. Wu, *J. Alloys Compd.*, 2016, **689**, 759.



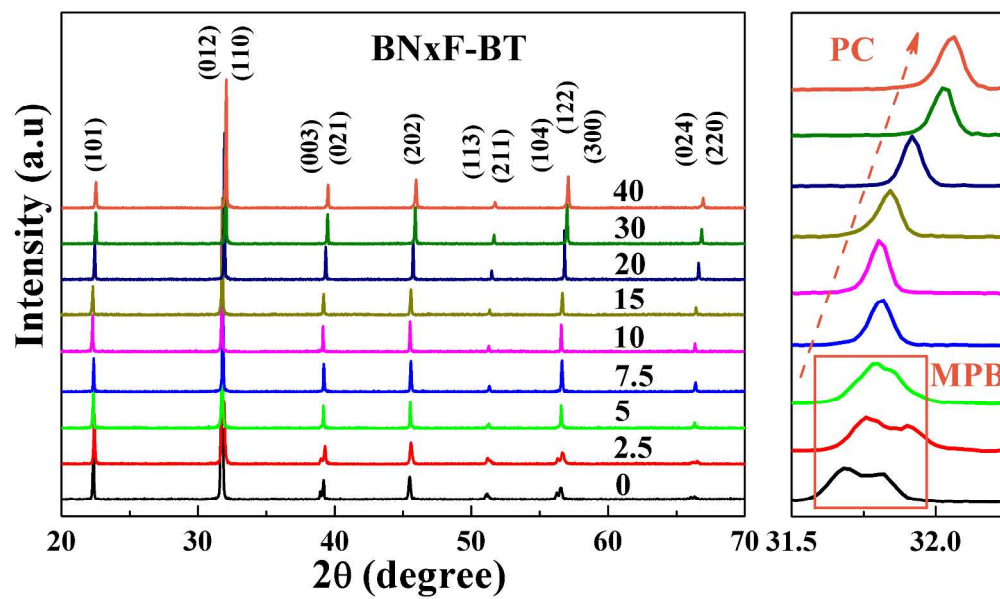


Fig. 1. RT XRD patterns of BN<sub>x</sub>F-BT in the 2θ range of 20°~70°.

289x171mm (300 x 300 DPI)

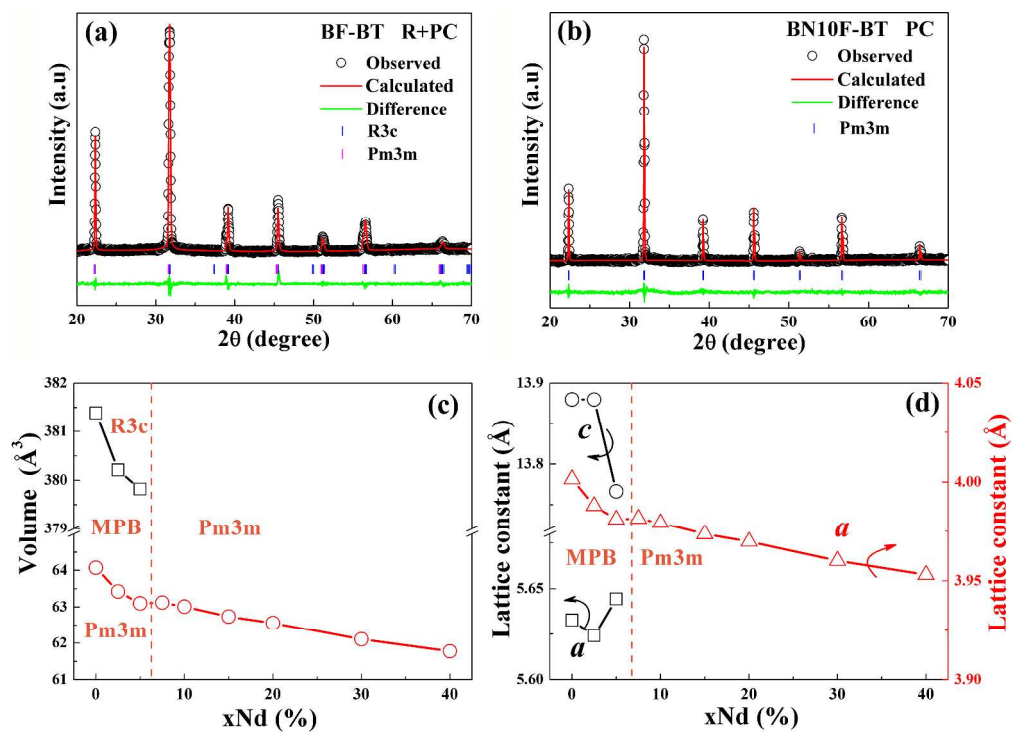


Fig. 2. Rietveld refinement analysis of (a) BF-BT and (c) BN10F-BT using the GSAS+EXPGUI package; (c) unit cell volume and (d) lattice parameters of  $\text{BN}_x\text{F-BT}$  as a function of Nd concentration. Error bars are smaller than the symbols.

496x356mm (300 x 300 DPI)

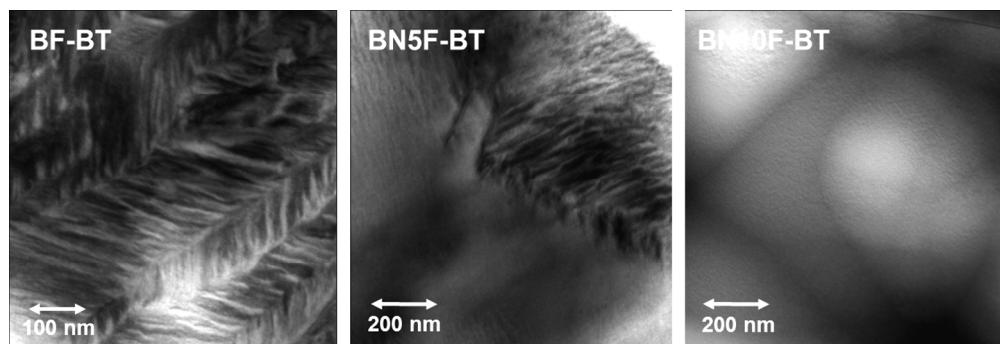


Fig. 3. TEM images of the domain structure in BF-BT, BN5F-BT and BN10F-BT.

234x79mm (149 x 149 DPI)

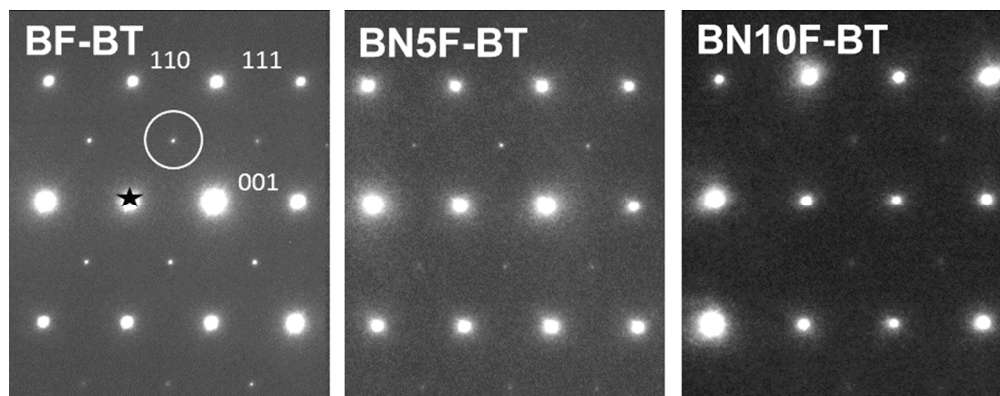


Fig. 4.  $\langle 110 \rangle$  zone axis diffraction patterns illustrating the decrease in intensity of  $\frac{1}{2}\{000\}$  antiphase tilt reflection as a function of increasing Nd concentration.

161x63mm (149 x 149 DPI)

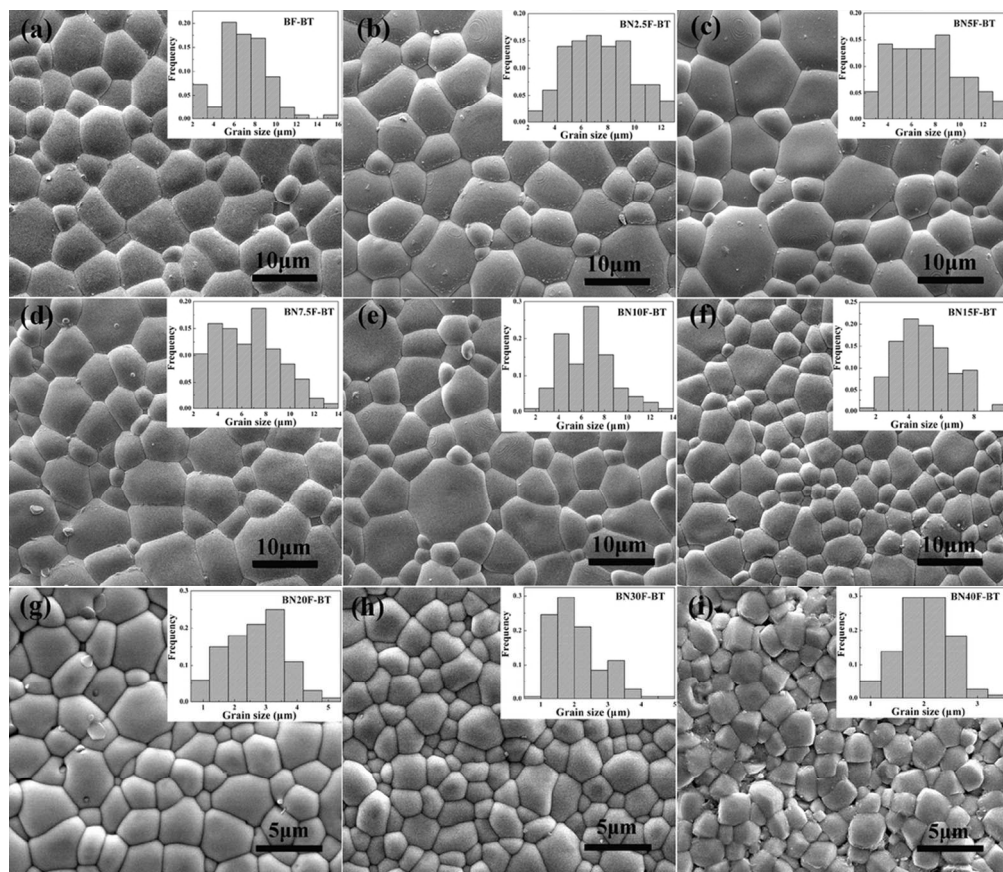


Fig. 5. SEM images of BN<sub>x</sub>F-BT with different Nd concentration: (a) BF-BT, (b) BN<sub>2.5</sub>F-BT, (c) BN<sub>5</sub>F-BT, (d) BN<sub>7.5</sub>F-BT, (e) BN<sub>10</sub>F-BT, (f) BN<sub>15</sub>F-BT, (g) BN<sub>20</sub>F-BT, (h) BN<sub>30</sub>F-BT and (i) BN<sub>40</sub>F-BT; The grain size distributions of BN<sub>x</sub>F-BT are in the insets of each SEM images.

95x82mm (300 x 300 DPI)

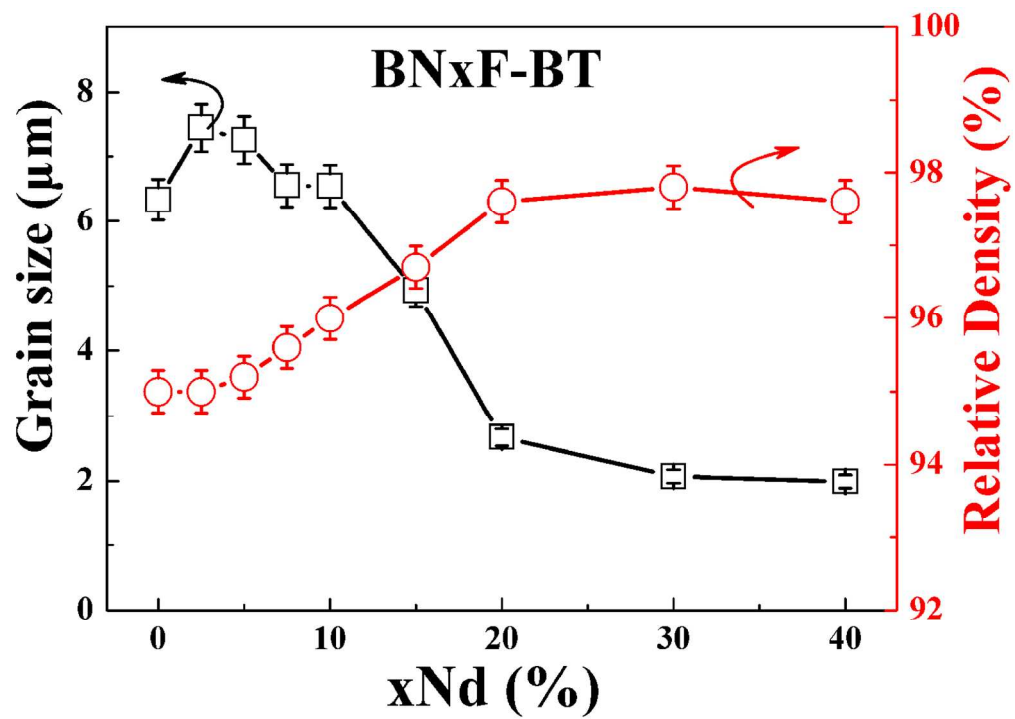


Fig. 6. Average grain size and relative density of BN<sub>x</sub>F-BT as a function of Nd concentration.

127x90mm (300 x 300 DPI)

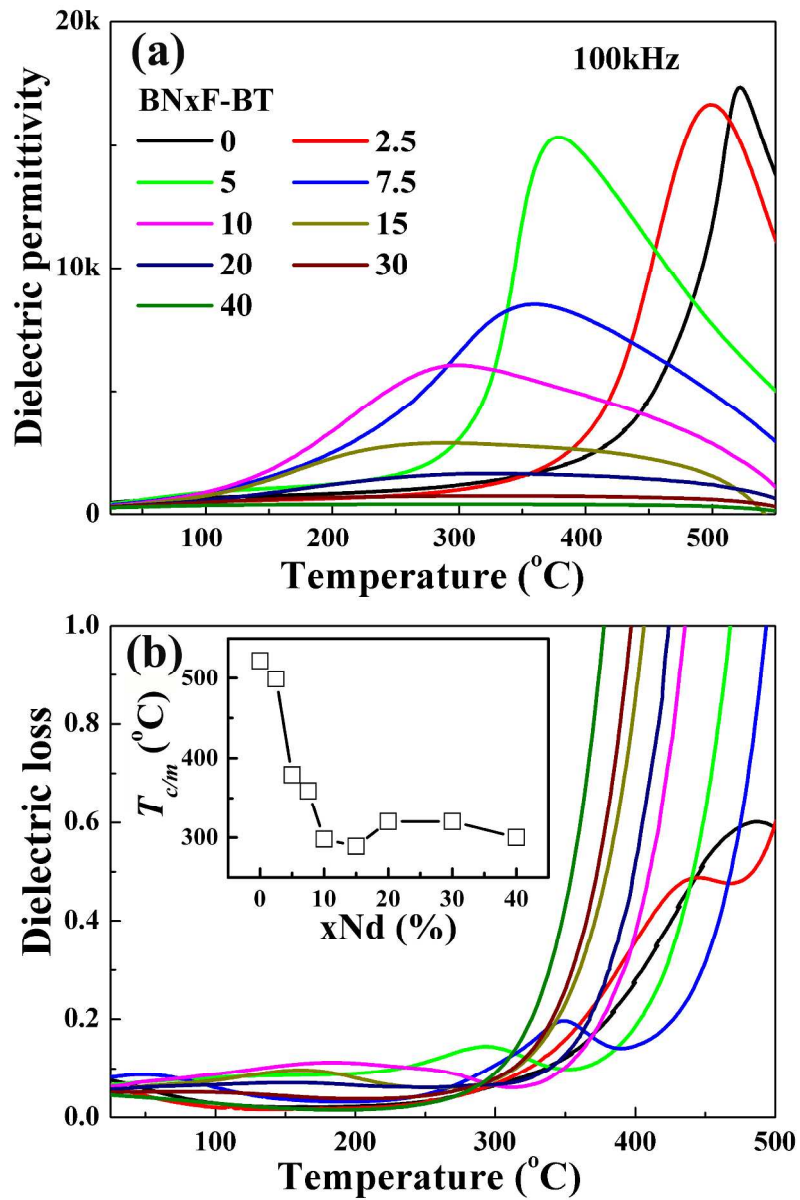


Fig. 7. Temperature dependence of (a)  $\epsilon_r$  and (b)  $\tan\delta$  for BN<sub>x</sub>F-BT; TC/T<sub>m</sub> as a function of Nd concentration is in the inset of (b). Note. Error bars are smaller than the symbols.

234x356mm (300 x 300 DPI)

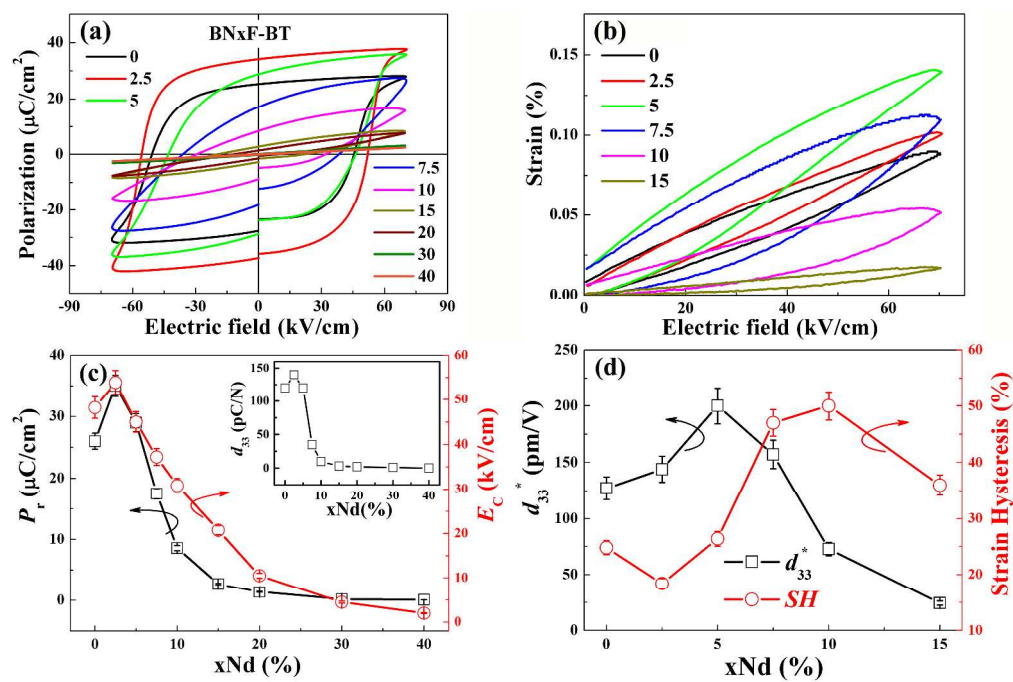


Fig. 8. High electric field (a) bipolar polarization hysteresis loops and (b) unipolar strain loops for BNxFT-BT; (c) corresponding  $P_r$  and  $E_c$  as a function of Nd concentration; (d) corresponding  $d_{33}^*$  and SH as a function of Nd concentration;  $d_{33}$  as a function of Nd concentration is in the inset of (c).

523x352mm (300 x 300 DPI)



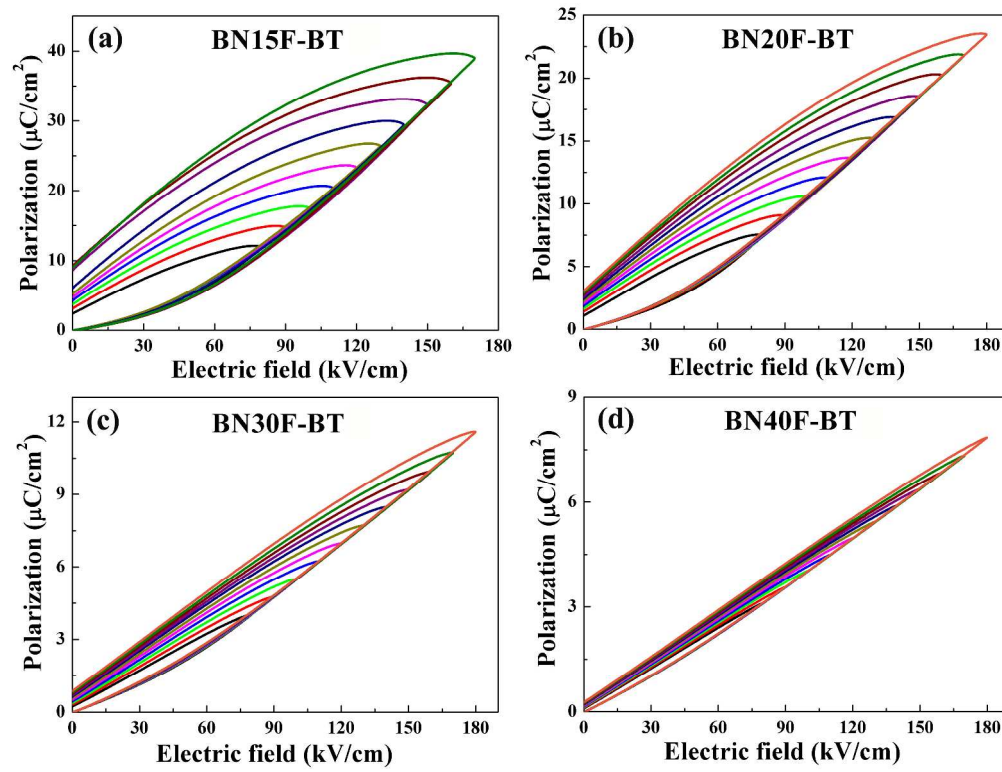


Fig. 9. Unipolar P-E loops under different electric fields for (a) BN15F-BT, (b) BN20F-BT, (c) BN30F-BT and (d) BN40F-BT.

464x356mm (300 x 300 DPI)

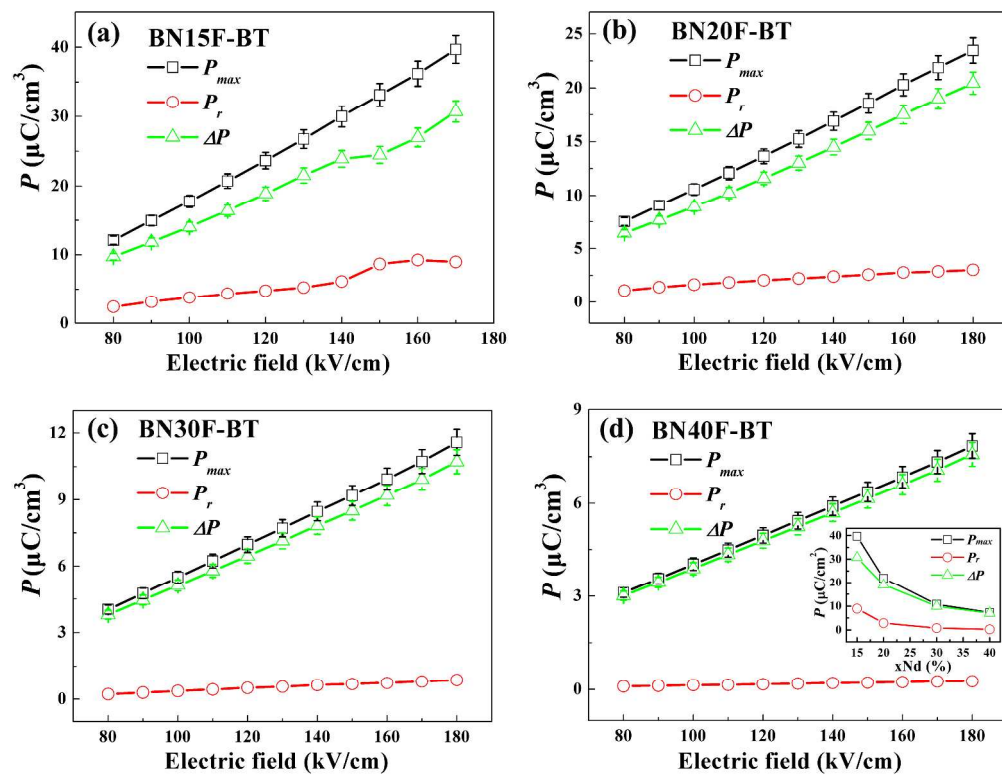


Fig. 10.  $P_{max}$ ,  $P_r$  and  $\Delta P$  as a function of electrical field for (a) BN15F-BT, (b) BN20F-BT, (c) BN30F-BT and (d) BN40F-BT;  $P_{max}$ ,  $P_r$  and  $\Delta P$  as a function of Nd concentration at 170  $\text{kV}/\text{cm}$  is in the inset of (d).

472x361mm (300 x 300 DPI)

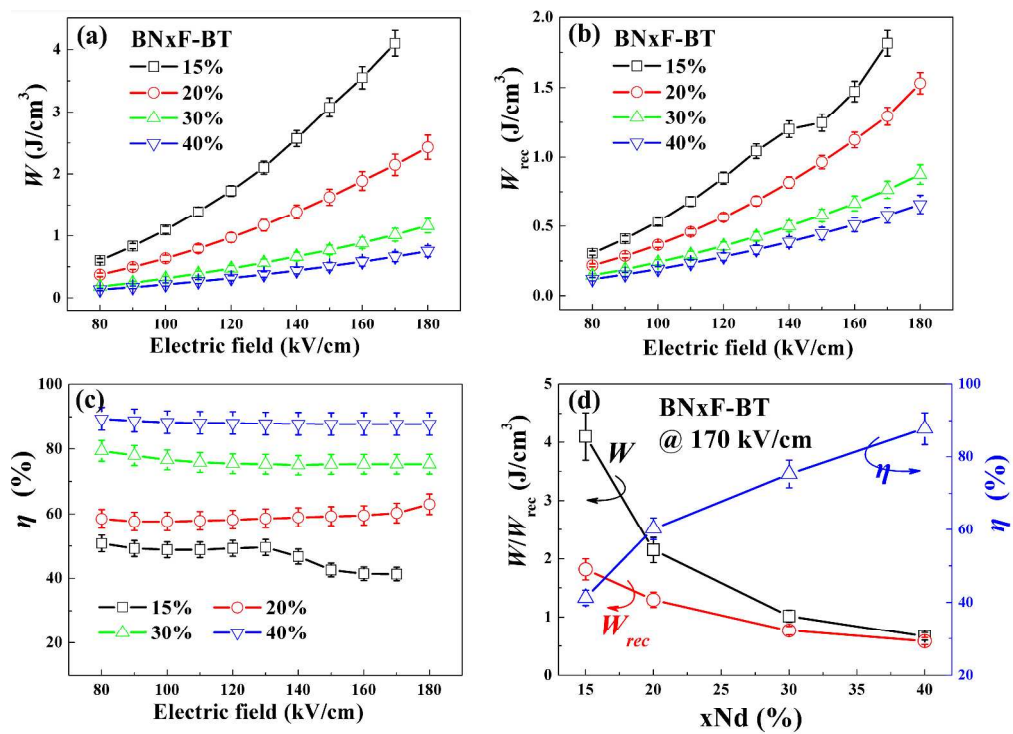


Fig. 11. (a)  $W$ , (b)  $W_{rec}$  and (c)  $\eta$  of BN15F-BT, BN20F-BT, BN30F-BT and BN40F-BT as a function of electrical field; (e)  $W$ ,  $W_{rec}$  and  $\eta$  as a function of Nd concentration at 170 kV/cm.

502x363mm (300 x 300 DPI)

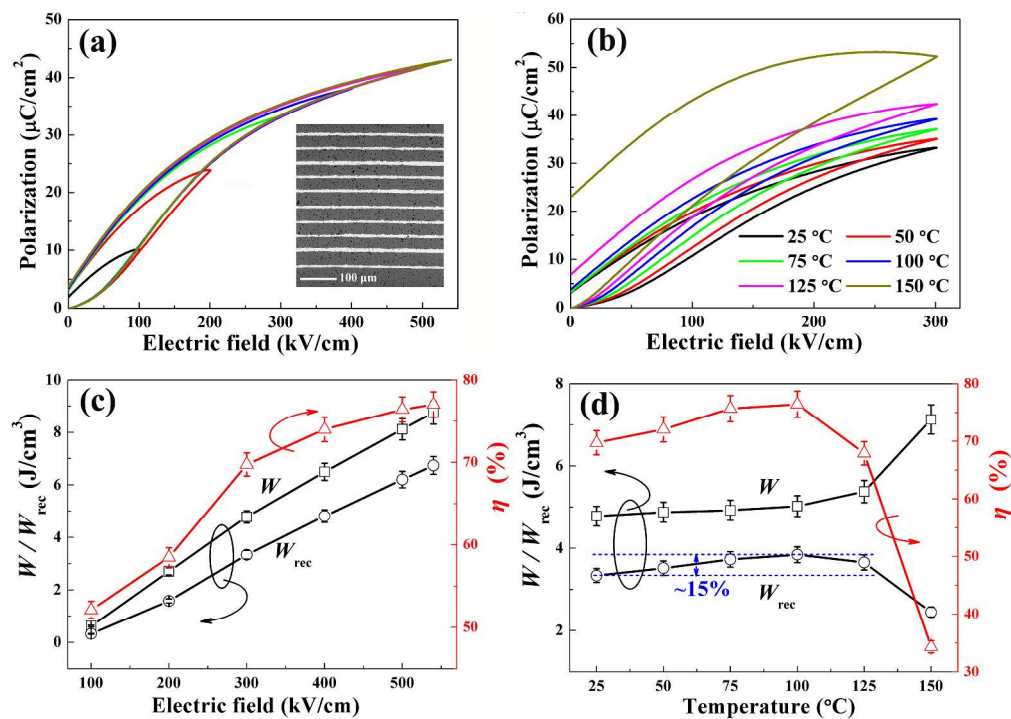


Fig. 12. (a) Unipolar P-E loops of multilayers under different electric fields at RT, (b) in-situ temperature dependence of unipolar P-E loops of multilayers at an electric field of 300 kV/cm, (c)  $W$ ,  $W_{\text{rec}}$  and  $\eta$  of multilayers as a function of electric field at RT, and (d)  $W$ ,  $W_{\text{rec}}$  and  $\eta$  of multilayers as a function of temperature at 300 kV/cm; SEM image of multilayers is in the inset of (a).

338x239mm (300 x 300 DPI)

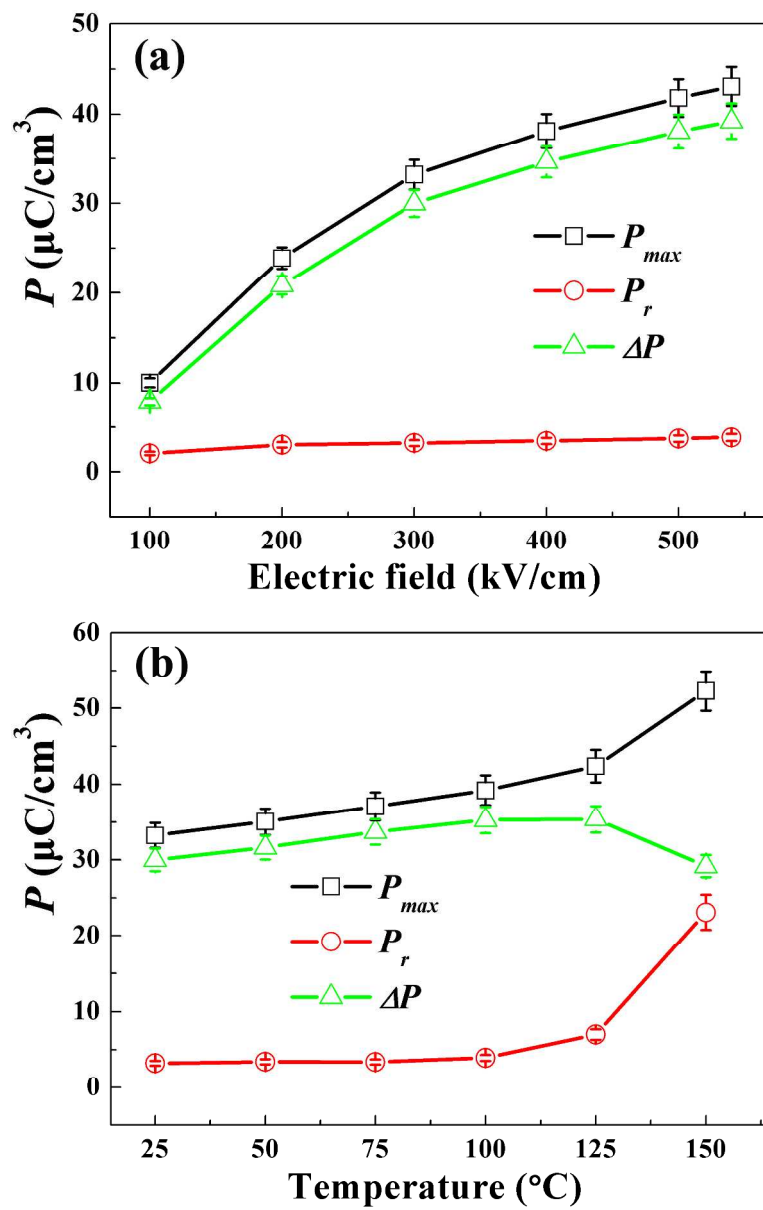


Fig. 13.  $P_{max}$ ,  $P_r$  and  $\Delta P$  of multilayers (a) as a function of electrical field at RT and (b) as a function of temperature at 300 kV/cm.

229x358mm (300 x 300 DPI)

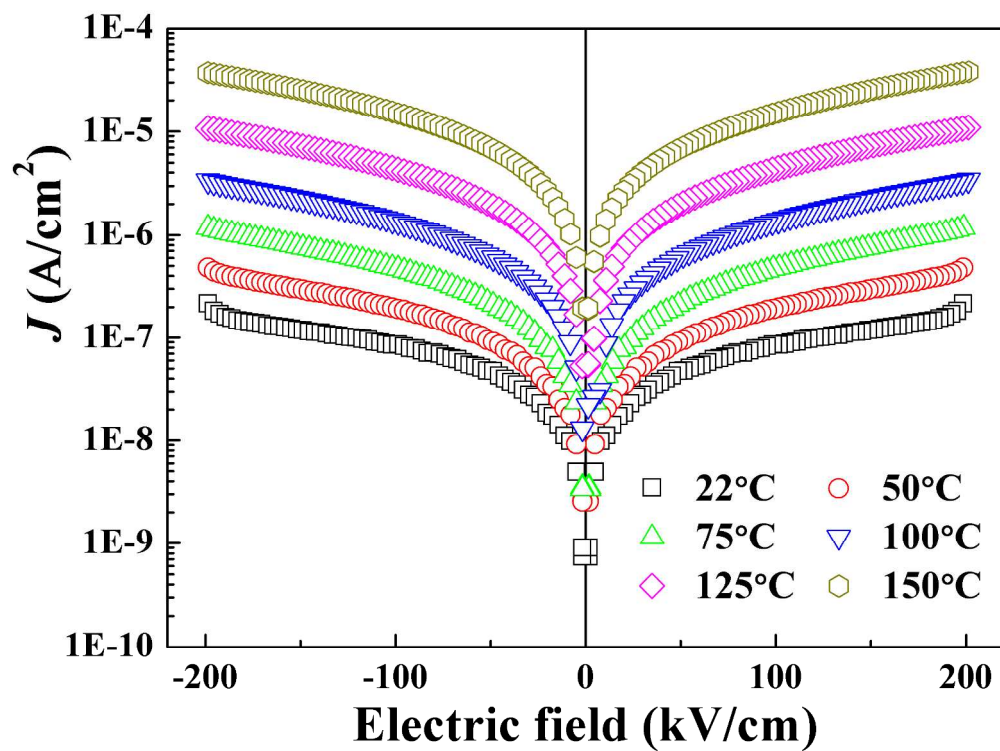


Fig. 14. The in-situ temperature dependence of leakage current density ( $J$ ) of multilayers as a function of applied field.

236x175mm (300 x 300 DPI)

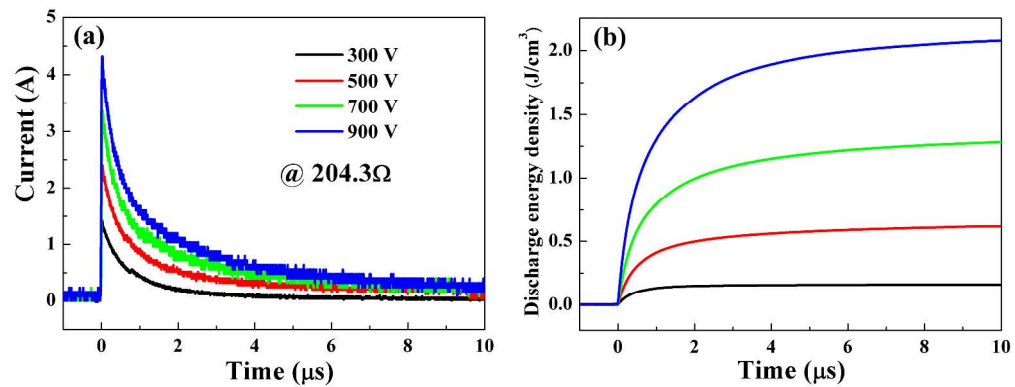


Fig. 15. The discharging behaviour of multilayers under different electric voltages (a) time dependence of the pulsed discharge current and (b) time dependence of the discharge energy density.

469x178mm (300 x 300 DPI)

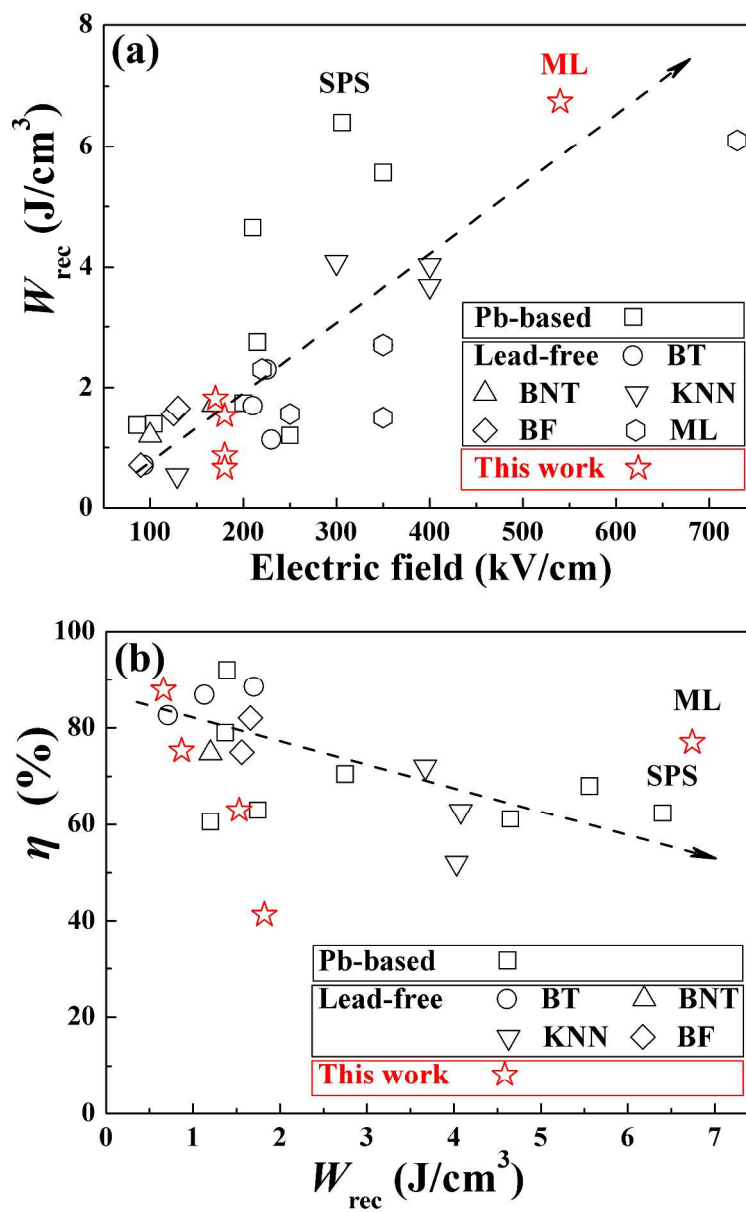


Fig. 16. Comparison of energy-storage properties among lead-based and lead-free ceramics/capacitors. 10-15, 19-31, 36-38, 56-60, 63

227x363mm (300 x 300 DPI)



**Table I.** Refined structural parameters of BN<sub>x</sub>F-BT ceramics.

Composition x	Space group	Lattice parameters (Å)			Volume (Å <sup>3</sup> )	Phase fraction (%)	R factors (%)		
		a	b	c			$R_{wp}$	$R_p$	$\chi^2$
0	<i>R3c</i>	5.6328	5.6328	13.8800	381.389	65.2 <sup>R</sup>	9.6	7.3	1.8
	<i>Pm3̄m</i>	4.0015	4.0015	4.0015	64.073	34.8 <sup>C</sup>			
2.5	<i>R3c</i>	5.6241	5.6241	13.8798	380.209	37.8 <sup>R</sup>	9.9	7.5	3.7
	<i>Pm3̄m</i>	3.9880	3.9880	3.9880	63.425	62.2 <sup>C</sup>			
5	<i>R3c</i>	5.6444	5.6444	13.7664	379.821	27.9 <sup>R</sup>	8.7	6.9	1.8
	<i>Pm3̄m</i>	3.9812	3.9812	3.9812	63.100	72.1 <sup>C</sup>			
7.5	<i>Pm3̄m</i>	3.9816	3.9816	3.9816	63.121		10.3	8.2	2.0
10	<i>Pm3̄m</i>	3.9793	3.9793	3.9793	63.012		8.6	6.6	1.8
15	<i>Pm3̄m</i>	3.9736	3.9736	3.9736	62.739		8.8	6.9	1.7
20	<i>Pm3̄m</i>	3.9698	3.9698	3.9698	62.563		9.9	7.4	1.5
30	<i>Pm3̄m</i>	3.9602	3.9602	3.9602	62.107		10	7.5	1.6
40	<i>Pm3̄m</i>	3.9531	3.9531	3.9531	61.777		10.9	7.9	1.8

**Table II.** Comparison of polarization and energy storage properties among lead-free ceramics.

Compounds	$E$ (kV/cm)	$P_{max}$ ( $\mu\text{C}/\text{cm}^2$ )	$\Delta P_r$ ( $\mu\text{C}/\text{cm}^2$ )	$W$ ( $\text{J}/\text{cm}^3$ )	$W_{rec}$ ( $\text{J}/\text{cm}^3$ )	$\eta$ (%)	Ref
BF-BT-Nb	90	25	19.7	/	0.71	/	36
BF-BT-BMN	125	38	32.3	2.08	1.56	75	37
BF-BT-LMT	130	37.5	33.3	2.02	1.66	82	38
BT-BMN	210	21	16.3	1.92	1.7	88.5	23
BT-BY	93	~17	~16	0.86	0.71	82.6	26
BST	230	~12	~11	1.3	1.13	86.8	56
BNT-BT-KN	168	~40	~30	/	1.72	/	28
BNT-BT-NT	100	~33	~29	1.6	1.2	74.8	29
KNNS-BNH	129	23.47	18.61	/	0.54	/	61
KNN-BMN	300	~41.7	~33.7	6.5	4.08	62.8	30
KNN-ST	400	33.3	~16	7.76	4.03	52	31
BN15F-BT	170	39.8	30.7	4.1	1.82	41.3	this work
BN20F-BT	180	23.5	20.4	2.43	1.53	63	this work
BN30F-BT	180	11.6	10.7	1.16	0.87	75.3	this work
BN40F-BT	180	7.8	7.6	0.75	0.66	87.8	this work

Bismuth ferrite-based lead free multilayers with high recoverable energy density of  $6.74 \text{ J/cm}^3$  and efficiency of 77%, stable up to  $125^\circ\text{C}$ .

